Densely populated trimetallic single-atoms for durable low-temperature flexible zinc-air batteries

Wenfang Zhai [a], Yuting He [a], Yu-e Duan [b], Shengwu Guo [a], Yuanzhen Chen [a], Zhengfei Dai [a], Liting Liu [c,*], Qiang Tan [a,*]

[a] *State Key Laboratory for Mechanical Behavior of Materials, Xi'an Jiaotong University, Xi'an, Shaanxi 710049, PR China*
[b] *School of Chemistry and Chemical Engineering, Xi'an University of Science and Technology, Xi'an, Shaanxi 710054, PR China*
[c] *Analytical and Testing Center, Northwestern Polytechnical University, Xi'an, Shaanxi 710072, PR China*

ARTICLE INFO

ABSTRACT

The fundamental challenge of trimetallic single-atoms catalysts stems from the difficulty in supporting the coexistence of different metals with their unique physicochemical features. Here, the trimetallic single-atoms electrocatalyst is constructed as a model system to explore electrocatalytic ORR/OER. The tri-metal (Fe, Co, and Ni) single-atoms loaded on nitrogen-carbon framework exhibits superior ORR/OER kinetics ($E_{1/2}$ = 0.927 V, $E_{j=10}$ = 1.56 V). The flexible zinc-air batteries generate excellent power density and durability (62 mW cm^{-2} and 200 h at −15 °C, 291.2 mW cm^{-2} and 250 h at room temperature). Density functional calculations confirm that the trimetallic synergy effect outperform mono- and bimetallic effects, yielding adsorption strength close to 0. This paper describes an intuitionistic descriptor where ΔE_{OH*} displays a volcano relationship with ORR overpotential, and establishes a generalized strategy for efficient bifunctional oxygen electrocatalyst while comprehensively understanding the structure-mechanism-activity relationship.

1. Introduction

Flexible electronics, as opposed to traditional electronics, offer a broad range of applications in information, energy, medicine, national security, and other fields [1,2]. To address the need for portable electronics, flexible electronics have been developed by electronic brands and researchers worldwide due to their distinctive flexibility, ductility, portability, high efficiency, and low-cost manufacturing process [3,4]. Flexible Zinc-air batteries (FZABs), as a clean energy storage device, have attracted much attention because of their high energy density (5 times that of lithium-ion battery), lightweight, no electrolyte leakage, cheap raw materials, excellent foldability, and non-polluting characteristics [5–8]. Nevertheless, the oxygen reduction and oxygen evolution reaction (ORR/OER) at FZABs cathode undergoes a complex and kinetic sluggish 4-electron (4e$^-$, O$_2$ ⇋ OH$^-$) conversion process, which limits the rate capability and cycle life of the practical FZABs [9–12]. Considerable efforts have been devoted to combating the sluggish kinetics, a promising strategy has been typically employed that uses the single-atom (SA) bifunctional oxygen electrocatalysts to accelerate the kinetics of the ORR/OER process, and which further led to improve the electrochemical performance of the FZABs [13–18].

Single-atom bifunctional oxygen electrocatalysts possess superior catalytic properties due to their dramatically increased surface free energy, quantum size effect, unsaturated coordination environment, and metal-support interactions [19,20]. Yet, SA catalysts with one type of metal site only can catalyze the partial reactions with a single active center, and they are helpless on catalyzing the reactions with multi-sites synergy [21–23]. Furthermore, single-atom catalysts adsorbed directly onto the support can easily migrate and become agglomerated and deactivated [24–26]. Bifunctionality, activity, and stability of established bimetallic SA catalysts remain unsatisfactory. The research of trimetallic SA catalysts is motivated by the synergistic intermetallic effects in bimetallic SA catalysts [27]. The fundamental challenge of trimetallic SA catalysts stems from the difficulty in supporting the coexistence of different metals with their unique physicochemical features. The coexistence of multiple metals in high-entropy alloys brings a blueprint for the construction of trimetallic SA catalysts. Given that, selection of suitable metals leads to trimetallic SA catalysts with zero adsorption strength for oxygenated intermediates. Thus, one of the strategies for achieving high activity and extended longevity FZABs is

---

the development of single-atom oxygen bifunctional electrocatalysts of multi-metal species.

Herein, we reported a systematic investigation of multi-transition metal SA (M-TM SA) oxygen bifunctional electrocatalysts for application in FZABs. To understand the catalytic performance of various M-TM SA loaded on nitrogen-carbon framework (NC) electrocatalysts and their impact on battery performance, we focus on fundamental electrocatalytic studies by systematically probing the ORR/OER activity, stability, reaction kinetics, and reaction mechanisms. Within this system, which consists of different content Fe, Co, and Ni loaded on NC, the $Fe_{3\%}Co_{3\%}Ni_{9\%}$-NC-1000 (x% represents the molar ratio of metal to Zn in ZIF8, 1000 means the heat treatment is 1000 °C) exhibits superior ORR/OER catalytic activity ($E_{1/2} = 0.927$ V, $E_{j=10} = 1.56$ V) with considerably improved kinetics in alkaline electrolyte. Furthermore, the $Fe_{3\%}Co_{3\%}Ni_{9\%}$-NC-1000 was assembled FZABs, attained more stable open-circuit voltage ($\approx$1.5 V), superior power density (62.2 mW cm^{-2} for −15 °C, 291.2 mW cm^{-2} for 25 °C), and durable cycle performance (200 h for −15 °C, over 250 h for 25 °C). The two FZABs in series based on $Fe_{3\%}Co_{3\%}Ni_{9\%}$-NC1000 electrocatalysts can light up a number of small LED bulbs with a rated voltage of 3 V. This work provides a new strategy for the M-TM SA oxygen bifunctional electrocatalysts for clean energy storage devices.

2. Experimental section

2.1. Chemical

Zinc nitrate hexahydrate ($Zn(NO_3)_2 \cdot 6H_2O$, 99%), ferrous nitrate hexahydrate ($Fe(NO_3)_2 \cdot 6H_2O$, 99%), cobalt nitrate hexahydrate (Co $(NO_3)_2 \cdot 6H_2O$, 99%), nickel nitrate hexahydrate ($Ni(NO_3)_2 \cdot 6 H_2O$, 99%), 2-methylimidazole, methanol, isopropyl alcohol (98%), 5 wt% Nafion solution, potassium hydroxide (KOH), 40 wt% Pt/C, ruthenium oxide (RuO_2), acrylic acid (AA, 99%) solution, N, N′-methylene-bis-acrylamide (MBA) and Potassium persulfate ($K_2S_2O_8$), were purchased from Aladdin Industrial Corporation. Deionized water was obtained from an ultrapure purification system (Ultrapure, resistivity $\geq$ 18.25 MΩ). The zinc foil was obtained from Alfa Aesar. All chemical reagents were used without any further purification.

2.2. Synthesis of the $Fe_xCo_yNi_z$-NC catalysts

A series of $Fe_xCo_yNi_z$-NC catalysts were made based on ZIF8. X, y, z represent the molar ratio of Fe, Co, and Ni to Zn in ZIF8, respectively. Take the synthesis of $Fe_{3\%}Co_{3\%}Ni_{9\%}$-NC as a typical example. Firstly, 10 mmol $Zn(NO_3)_2 \cdot 6H_2O$, 0.3 mmol $Fe(NO_3)_2 \cdot 6H_2O$, 0.3 mmol Co $(NO_3)_2 \cdot 6H_2O$ and 0.9 mmol $Ni(NO_3)_2 \cdot 6H_2O$ were dissolved into 300 mL methanol (Solution A) and 3.94 g 2-methylimidazole was dissolved into 300 mL methanol (Solution B), respectively. Solution A and solution B were stirred magnetically for 30 min and then mixed together (Solution C). Solution C was reacted in a 60 °C constant temperature oven for 24 h. The reaction solution was centrifuged and cleaned with methanol several times. After that, the washed precursor was put into the freeze dryer to dry for 12 h. Finally, grind the dried precursor evenly, place it in a quartz boat and burn it in a tubular furnace at 900, 1000, 1100 °C for 1 h, respectively. The synthesis procedures of other $Fe_xCo_yNi_z$-NC were identical by adjusting the weight of the used $Fe(NO_3)_2 \cdot 6H_2O$, Co $(NO_3)_2 \cdot 6H_2O$ and $Ni(NO_3)_2 \cdot 6H_2O$.

3. Results and discussion

3.1. Preparation and structural characterization of $Fe_xCo_yNi_z$-NC

Fig. 1a illustrates the synthetic scheme of $Fe_xCo_yNi_z$-NC catalysts. ZIF8 and $Fe_{3\%}Co_{3\%}Ni_{9\%}$-ZIF8 were synthesized via a solvothermal
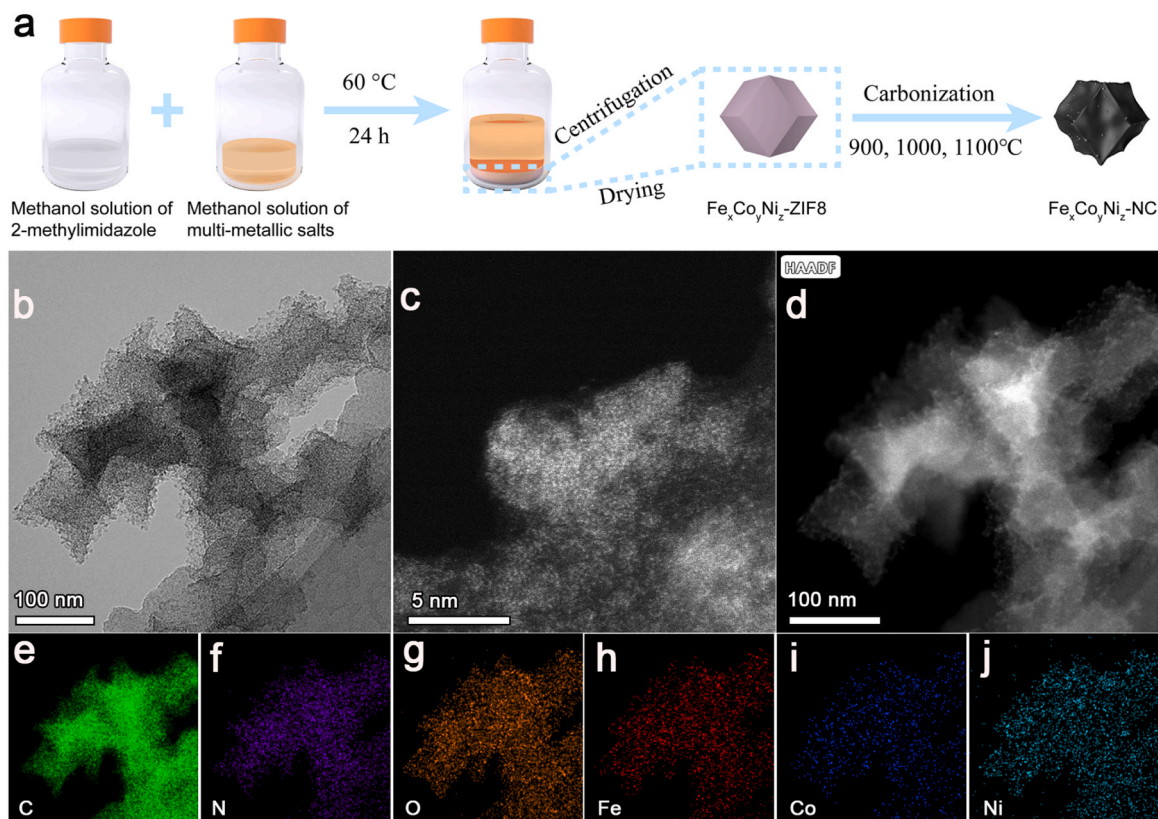
Fig. 1. a) Synthetic route of $Fe_xCo_yNi_z$-NC. Morphological and structural information of $Fe_{3\%}Co_{3\%}Ni_{9\%}$-NC1000. b) TEM. c) AC-STEM image. d) AC HADDF-STEM, e-j) The corresponding elementary mapping images of C, N, O, Fe, Co, and Ni.

method at 60 °C and reached uniform size with dodecahedron structure (Fig. S1) [10]. To form a nitrogen-carbon framework (NC), Fe$_{3\%}$Co$_{3\%}$Ni$_{9\%}$-ZIF8 was heat treated at 900 °C, 1000 °C, and 1100 °C, respectively. The structure of the Fe$_{3\%}$Co$_{3\%}$Ni$_{9\%}$-NC1000 was further characterized by scanning electron microscopy (SEM) and transmission electron microscopy (TEM). The SEM images (Fig. S2) show that the prepared Fe$_{3\%}$Co$_{3\%}$Ni$_{9\%}$-NC900, 1000, and 1100 materials present a collapsed dodecahedron structure and the statistical results show that the average diameter of the Fe$_{3\%}$Co$_{3\%}$Ni$_{9\%}$-NC1000 is approximately 87.16 nm. The TEM images of Fe$_{3\%}$Co$_{3\%}$Ni$_{9\%}$-NC1000 (Fig. 1b and S3) demonstrate that the Fe$_{3\%}$Co$_{3\%}$Ni$_{9\%}$-NC1000 still remains dodecahedron shape after pyrolysis and that no metal nanoparticles have formed [28,29]. Furthermore, the graphitic-like carbon structure with red cycles (d = 0.34 nm) was investigated in high-resolution TEM (HRTEM), indicating the formation of a short-range ordered carbon structure during the heat treatment (Fig. S3c) [30]. The aberration-corrected high-angle annular dark-field scanning transmission electron microscope (AC HAADF-STEM) was conducted to analyze atomic metal site morphologies of the Fe$_{3\%}$Co$_{3\%}$Ni$_{9\%}$-NC1000 (Fig. 1c). High-density, well-dispersed single-atom metal sites are identified and widely dispersed in a carbon matrix, similar to other works [31,32]. Moreover, the TEM elemental mapping (Fig. 1d-j) clearly shows that uniform distribution of C, N, O, Fe, Co, and Ni throughout the dodecahedron structure, indicating successful heteroatom coordination to the structure of ZIF8 [33,34]. Elemental analysis of the Area#1 was also performed, and the atomic fraction and mass fraction of Fe, Co, and Ni elements were seen to be present in trace amounts (Fig. S4). The ICP-MS data in Table S1 showed the specific content of the elements Fe, Co, and Ni in the Fe$_{3\%}$Co$_{3\%}$Ni$_{9\%}$-NC1000 electrocatalyst. This result is consistent the elemental analysis of the Area#1, both of which indicated that the catalyst contains traces of metals.

X-ray diffraction (XRD) patterns of the Fe$_{3\%}$Co$_{3\%}$Ni$_{9\%}$-NC900, 1000, 1100 catalysts were conducted (Fig. 2a), indicating two peaks are located at 26° and 44°, which are the (002) and (101) crystal planes of amorphous graphitic carbon, respectively [35,36]. This result matches the short-range disordered graphitic carbon results shown in the previous TEM data (Fig. S3c). However, for Fe$_{3\%}$Co$_{3\%}$Ni$_{9\%}$-NC1100 sample, two peaks at 26° and 44° clearly indicate the generation of graphitic carbon with a well-crystalline phase. The absence of metal peaks in XRD can be assumed that metals are most likely present in the nitrogen-carbon framework at the atomic level. In the frequency range of 800–2000 cm^{-1}, Raman spectra (Fig. 2b) shows that the intensity ratio of D and G band on the Fe$_{3\%}$Co$_{3\%}$Ni$_{9\%}$-NC900, 1000, 1100 (I$_D$/I$_G$=1.10, 0.97, 0.92). The D-band peak is derived from the disorder or defects that existed in carbon lattice, and G-band peak is corresponded to the graphitic carbon, respectively [37]. With the increase in temperature, the value of I$_D$/I$_G$ becomes smaller, indicating that the degree of graphitization is higher. This phenomenon is consistent with HRTEM and XRD results.

To further characterize the chemical composition and bonding configuration, we carried out X-ray photoelectron spectroscopy (XPS) measurements. The C 1s peak at 284.6 eV was used to calibrate the spectrum (Fig. S5). The peak at 285.4 eV assigned to the bonding of C-N, proves the formation of N-doped carbon. Since the boiling point of zinc is 907 °C [38,39], we can only see a significant zinc peak at 900 °C, but not at 1000 °C and 1100 °C (Fig. 2c and Table S2). Additionally, the high-resolution N 1s spectrum (Fig. 2d and Table S3) of Fe$_{3\%}$Co$_{3\%}$Ni$_{9\%}$-NC1000 can be deconvoluted into five subpeaks located at 398.4 eV (pyridinic-N), 399.8 eV (Metal-N, M-N), 400.8 eV (pyrrolic-N), 402.2 eV (graphitic-N), and 405.2 eV (oxidized-N) [40]. As shown in Fig. S6, different N-species content varies with the heat treatment temperature. Previous studies claimed that pyridinic-N, pyrrolic-N, and graphitic-N are beneficial for boosting oxygen adsorption and reducing the ORR and OER overpotential through their excellent electron-accepting ability, while pyridinic-N and pyrrolic-N can serve as metal-coordination sites owing to their lone-pair electrons [41]. Therefore, there are likely synergistic active sites of pyridinic-N, pyrrolic-N, and graphitic-N to enhance the electrocatalytic activity of catalysts [42,43]. The high-resolution Fe, Co and Ni 2p spectra are shown in Fig. S7-9, showing the trace amounts of metal elements, consistent with the TEM elemental mapping. The surface areas and porosity of Fe$_x$Co$_y$Ni$_z$-ZIF8 were further characterized by Brunauer-Emmett-Teller (BET)
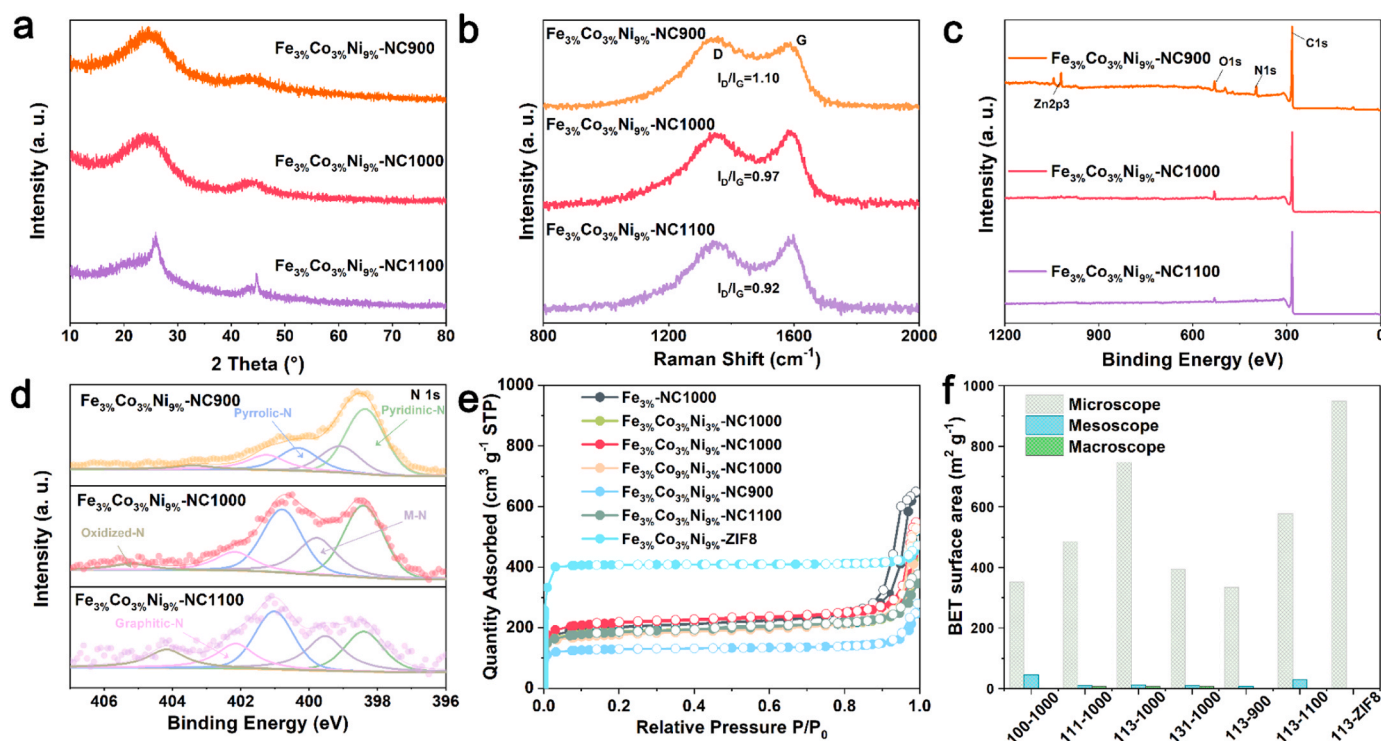

Fig. 2. a) XRD patterns. b) Raman spectrum. c) XPS survey. d) XPS N 1 s spectra. e) N$_2$ adsorption/desorption isotherms. f) Pore distribution of catalysts.

measurements. All the $Fe_xCo_yNi_z$-ZIF8 catalysts exhibit a type-VI N_2 adsorption-desorption isothermal [44], suggesting the existence of both micropores and mesopores (Fig. 2e). Surface area and pore distribution plots (Fig. 2f), suggesting the majority of the pore surface area is attributed to the micropore. Micropores can provide more active sites for the catalyst and improve its catalytic activity. Pore volume distribution graphs (Fig. S10) suggesting that $Fe_{3\%}Co_{3\%}Ni_{9\%}$-NC1000 has the highest specific surface area in the pyrolytic samples (SSA, 694.84 m^2 g^{-1}). Moreover, the distribution of pores changed due to the volatilization of zinc, forming a majority of mesopores and a portion of macropores, and forming a hierarchical porous structure. This highly porous structure of $Fe_{3\%}Co_{3\%}Ni_{9\%}$-NC1000 can provide effective diffusion path to active sites for electrolytes or intermediates, which facilitates the electrochemical reaction.

X-ray absorption near-edge structure (XANES) and extended X-ray absorption fine structure (EXAFS) analyses were further carried out to confirm the detailed structure information and local coordination information of $Fe_{3\%}Co_{3\%}Ni_{9\%}$-NC1000. Fig. 3a shows the Fe K-edge XANES spectra of the $Fe_{3\%}Co_{3\%}Ni_{9\%}$-NC1000 and comparative analysis with the results of Fe foil, FeO, Fe_2O_3, and FePc. XANES spectra exhibit

the intensity of the line for the $Fe_{3\%}Co_{3\%}Ni_{9\%}$-NC1000 situated between those for the Fe foil and FeO, further revealing the valence state of Fe is between 0 and +2, similar to FePc catalyst. The Fourier-transformed (FT) k^3-weighted EXAFS spectra of the R-space for the catalyst exhibit a dominant peak at 1.45 Å, ascribed to the Fe-N coordination peak (Fig. 3b) [45]. Metals (Fe, Co, and Ni) K-edge EXAFS (point) and the curvefit (line) of the R space (FT magnitude and imaginary component) and k space are shown in Fig. S11 and Fig. 3c, f, i. The fitting results agree well with the FeCoNiNC model in the DFT calculation. Detailed metals K-edge EXAFS fitting parameters can be found in Table S4. In the XANES spectra of Co (Fig. 3d), the results of comparison with Co foil, CoO, and Co_3O_4 indicate that the valence state of Co is between +2 and +3. The Fourier-transformed (FT) k^3-weighted EXAFS spectra of the catalyst R-space show a dominant peak at 1.3 Å, which can be identified as Co-N (Fig. 3e) [46]. The experimental and theoretical results for the Co-N scattering route are given in Fig. 3f. In the XANES spectra of Ni (Fig. 3g), the intensity of the line situated between those for the Ni foil and NiO, further revealing the valence state of Ni is between 0 and +2. The Fourier-transformed (FT) k^3-weighted EXAFS spectra of the R-space for the catalyst exhibit a dominant peak at 1.27 Å that can be
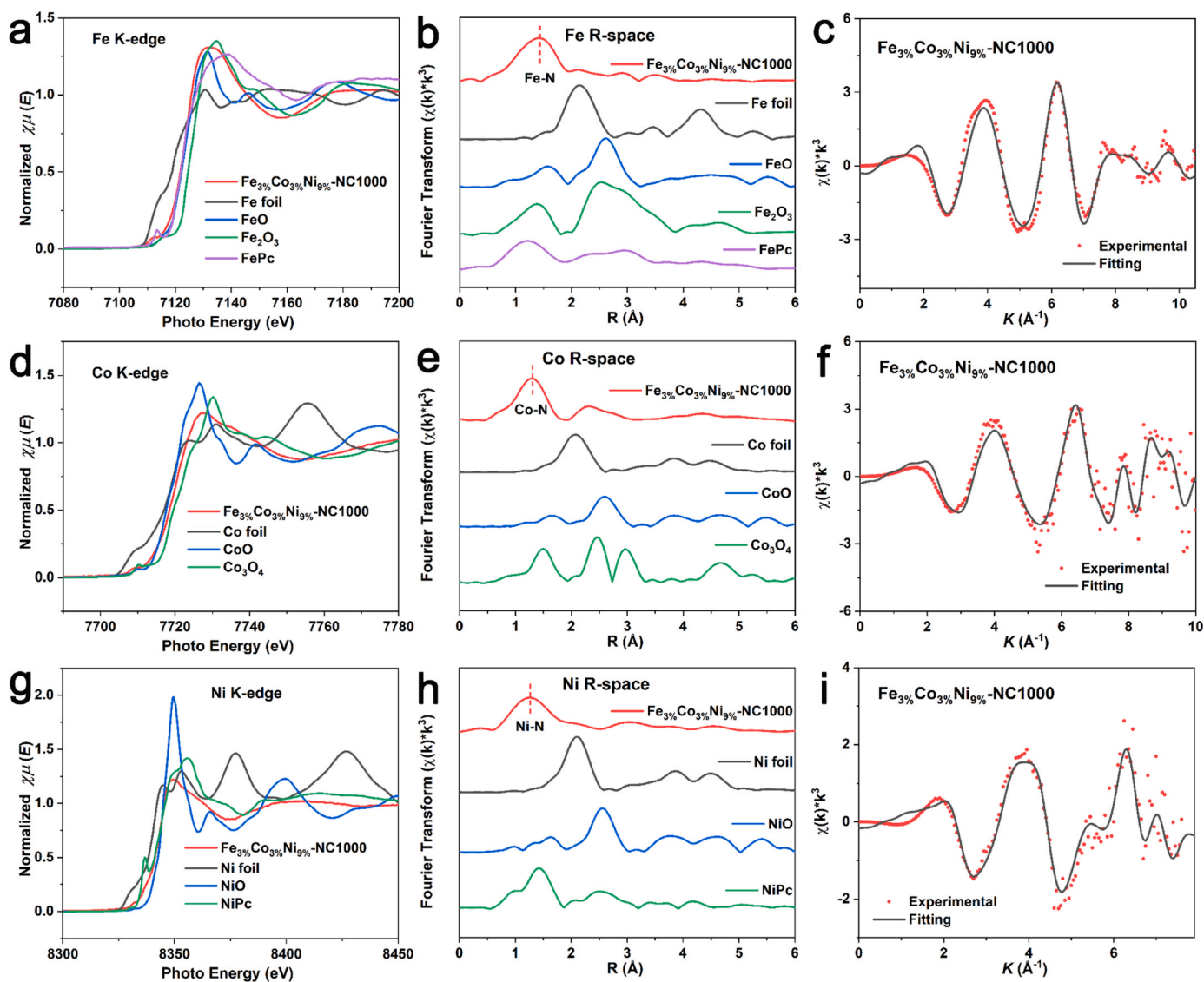

Fig. 3. a) Normalized Fe K-edge XANES spectra. b) k^3-weighted χ(k) function of the EXAFS spectra. c) EXAFS fitting curve of $Fe_{3\%}Co_{3\%}Ni_{9\%}$-NC1000. d) Normalized Co K-edge XANES spectra. e) k^3-weighted χ(k) function of the EXAFS spectra. f) EXAFS fitting curve of $Fe_{3\%}Co_{3\%}Ni_{9\%}$-NC1000. g) Normalized Ni K-edge XANES spectra. h) k^3-weighted χ(k) function of the EXAFS spectra. i) EXAFS fitting curve of $Fe_{3\%}Co_{3\%}Ni_{9\%}$-NC1000.

distinguished as Ni-N (Fig. 3h) [47]. The K-edge EXAFS fitting curves show that the experimental results were consistent with theoretical results when employing Ni-N scattering paths (Fig. 3i). The above results indicate the absence of metal-metal coordination, leading to the presence of the trimetallic single-atoms coordination structure. Combining the XAS findings (Fig. 3) with the AC HAADF-STEM image (Fig. 1c) of the catalysts, it can be claimed that the trimetallic single-atoms exhibit high density and excellent dispersion over the carbon matrix.

3.2. Electrocatalytic activities of $Fe_xCo_yNi_z$-NC for ORR and OER

Impressively, the bifunctional electrocatalytic properties of $Fe_xCo_yNi_z$-NC1000 and the benchmark catalysts (40 wt.% Pt/C, RuO_2) catalysts were evaluated by rotating ring-disk electrode (RRDE) measurements in a 0.1 M KOH solution with O_2-saturated. In the standard three-electrode system, a glassy carbon electrode with a mass loading of 1.47 mg cm^{-2} and a graphite rod were used as the working electrode and the counter electrode. All electrochemical tests were performed at room temperature. The cyclic voltammetry (CV) curves of three catalysts (Fig. 4a), indicating the current density at the peak of $Fe_{3\%}Co_{3\%}Ni_{9\%}$-NC1000 is significantly than that of $Fe_{3\%}Co_{3\%}Ni_{9\%}$-

NC900 and $Fe_{3\%}Co_{3\%}Ni_{9\%}$-NC1100, and that goes on to say that the $Fe_{3\%}Co_{3\%}Ni_{9\%}$-NC1000 has higher activity for ORR. Furthermore, the peak potential of $Fe_{3\%}Co_{3\%}Ni_{9\%}$-NC1000 is more positive (3 mV and 34 mV) than that of $Fe_{3\%}Co_{3\%}Ni_{9\%}$-NC900 and $Fe_{3\%}Co_{3\%}Ni_{9\%}$-NC1100. $Fe_{3\%}Co_{3\%}Ni_{9\%}$-NC1000 has the highest half-wave potential ($E_{1/2}$) of 0.927 V, which is more positive than that of 40 wt.% Pt/C at 0.863 V (Fig. 4b). The corresponding Tafel slope curves are shown in Fig. 4c, $Fe_{3\%}Co_{3\%}Ni_{9\%}$-NC1000 (84.6 mV dec^{-1}) has comparable kinetics to Pt/C (70.1 mV dec^{-1}) and has faster kinetic activity than the other prepared catalysts. Meanwhile, half-wave potentials of $Fe_xCo_yNi_z$-NC900, 1100 are not as excellent as $Fe_{3\%}Co_{3\%}Ni_{9\%}$-NC1000 (Fig. S12-14), indicating that the oxygen reduction reaction of the catalyst produced by the proportion and the pyrolysis temperature of $Fe_{3\%}Co_{3\%}Ni_{9\%}$-NC1000 was the best and the trimetallic single-atoms synergistic effect to increase its activity. Furthermore, the half-wave potentials of the bimetallic $Fe_{3\%}Co_{3\%}$-NC1000, $Fe_{3\%}Ni_{3\%}$-NC1000, and $Co_{3\%}Ni_{3\%}$-NC1000 are 0.89 V, 0.86 V, and 0.82 V, respectively, indicating that the trimetallic single-atoms synergistic is superior to bimetallic synergistic (Fig. S15). The EIS analysis was performed for the $Fe_{3\%}Co_{3\%}Ni_{9\%}$-NC1000 under different potentials in 1 M KOH solution to evaluate reduction efficiency in the potential range 1.0–0.4 V vs. RHE (Fig. S16). At the potential
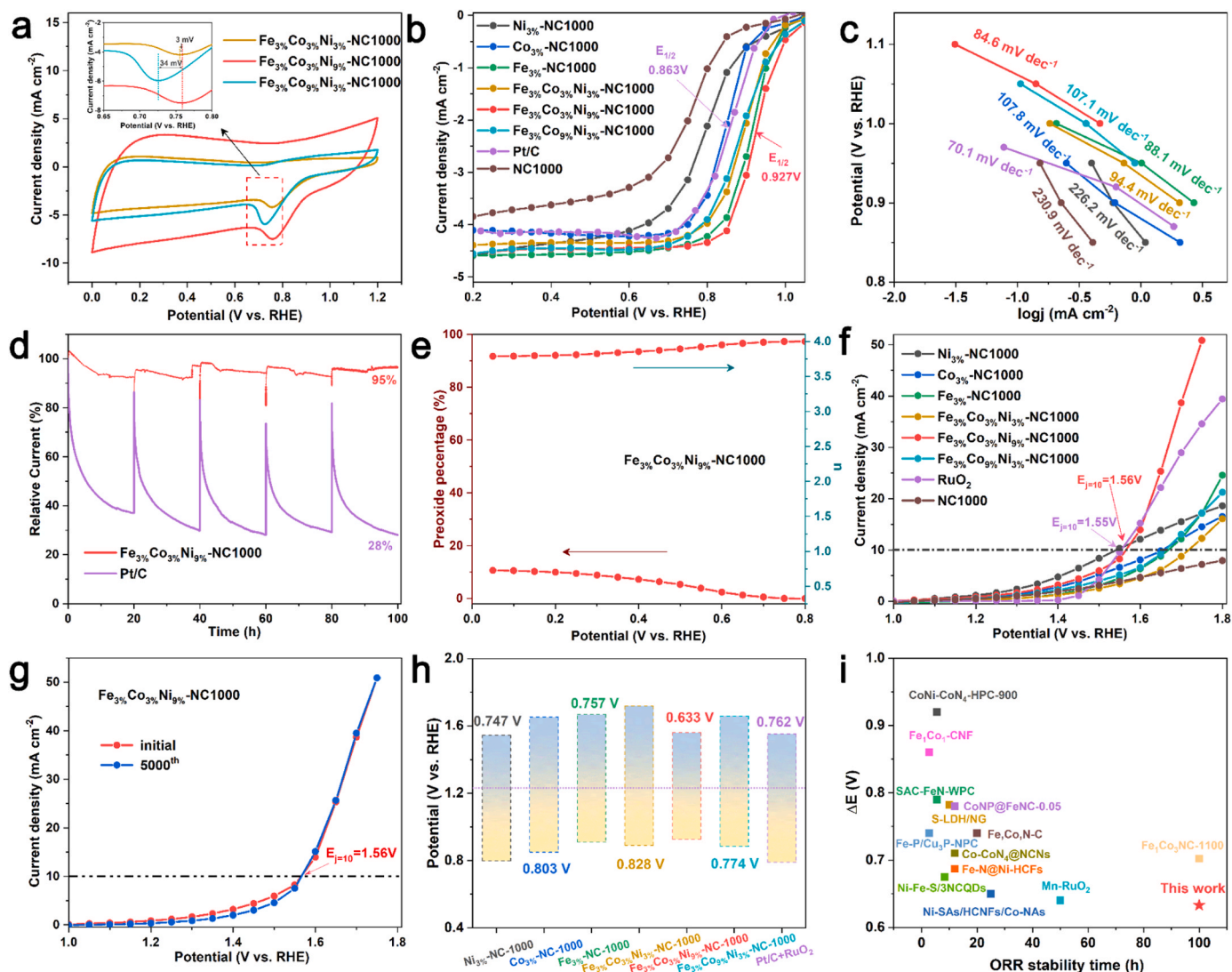
Fig. 4. ORR and OER performance of $Fe_xCo_yNi_z$-NC catalysts. a) CV curves at the scan rate of 50 mV s^{-1}. b) ORR curves. c) The corresponding Tafel slope of b). d) Chronoamperometric responses of $Fe_{3\%}Co_{3\%}Ni_{9\%}$-NC1000 and Pt/C during the ORR at a constant potential of 0.85 V. e) The H_2O_2 production yields and electron transfer number. f) OER curves. g) Long-term OER stability test of $Fe_{3\%}Co_{3\%}Ni_{9\%}$-NC1000 and RuO_2 at initial and after 5000th CV scanning. h) Comparison of ΔE (ΔE=1.23 V-(η_{10} +$E_{1/2}$)) of samples. i) Comparison the ΔE and ORR durability of $Fe_{3\%}Co_{3\%}Ni_{9\%}$-NC1000 and other reported bifunctional oxygen electrocatalysts.

higher than 0.9 V vs. RHE, R_{ct} is much higher, indicating weak charge transfer between the electrode and the reaction interface. When the potential at 0.9 V vs. RHE, the sharp decrease of R_{ct} suggests that direct oxygen reduction occurs on the electrode surface. When the potential is below 0.9 V vs. RHE, the sharp increase R_{ct} suggests H_2O formation and desorption from the electrode surface. More importantly, $Fe_{3\%}Co_{3\%}Ni_{9\%}$-NC1000 retained up to 95% of its original current after undergoing 100 h of continuous testing at 0.85 V (Figs. 4d and S17). In sharp contrast, the commercial 40 wt.% Pt/C electrode displayed a sharp reduction of the current by approximately 37%. The remarkable ORR activity and stability are strongly correlated to its densely populated tri-metal single-atom active sites, and the hierarchical porous structure of $Fe_{3\%}Co_{3\%}Ni_{9\%}$-NC1000 facilitates the diffusion of O_2 and electrolyte. The ORR linear sweep voltammetry (LSV) measurements of the $Fe_{3\%}Co_{3\%}Ni_{9\%}$-NC1000 under different rotating speeds and the corresponding Koutecky-Levich (K-L) plots at different potentials (vs RHE) (Fig. S18). As the rotating speed increases and as electrolyte

solubility decreases, the ORR limiting current density increases. The electron transfer number (n) is ≈ 3.9, which is consistent with the value of ≈ 4.0 derived from rotating ring-disk electrode (RRDE) measurements (Figs. 4e and S19). Additionally, the yield of H_2O_2 is below 10% in 0.1 M KOH solution (Fig. 4e). The above results illustrate an efficient four-electron ORR transfer pathway by the $Fe_{3\%}Co_{3\%}Ni_{9\%}$-NC1000.

Regarding the OER performance, the LSV curves of 10 mA cm^{-2} at an overpotential of only 330 mV, which is very close to that of RuO_2 (320 mV), and is much lower than other samples (Figs. 4f and S12–14). The corresponding Tafel slope curves are shown in Fig. S20, $Fe_{3\%}Co_{3\%}Ni_{9\%}$-NC1000 (90.7 mV dec^{-1}) has comparable kinetics to RuO_2 (75.6 mV dec^{-1}) and has faster kinetic activity than the other prepared catalysts. Nyquist plots for the OER over $Fe_{3\%}Co_{3\%}Ni_{9\%}$-NC1000 in the potential range 1.1–1.8 V vs. RHE, as presented in Fig. S21. As the potential increases, the impedance decreases, indicating that the oxygen evolution reaction proceeds more vigorously. The corresponding long-term CV cycling test for the $Fe_{3\%}Co_{3\%}Ni_{9\%}$-NC1000 and

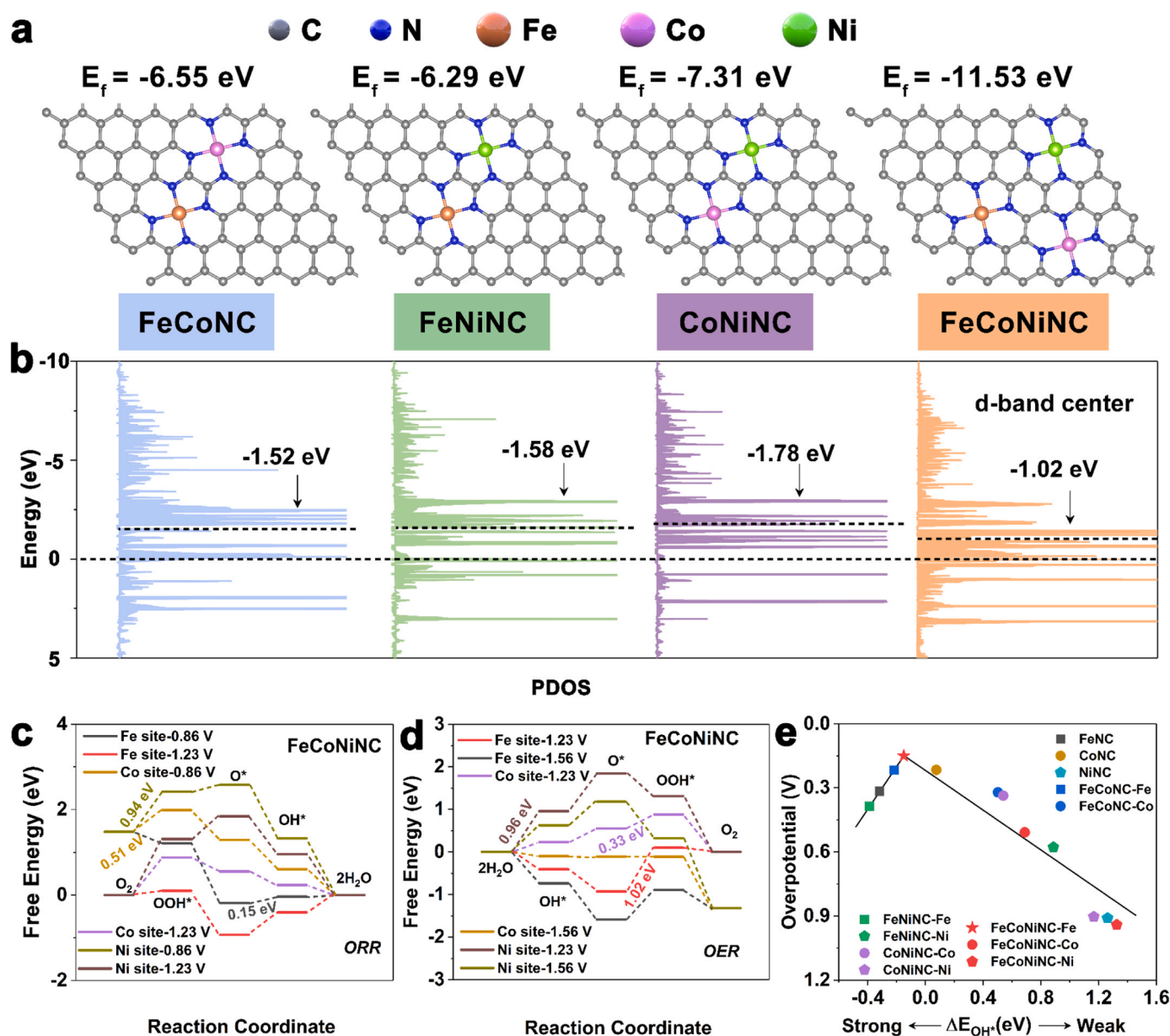**Fig. 5.** a) Atomic structures of electrocatalysts. The grey, blue, orange, purple, and green balls represent C, N, Fe, Co, and Ni atoms, respectively. b) Partial density of states (PDOS) and metal d-band center. c) Free energy for the ORR of FeCoNiNC in different metal-site. d) Free energy for the OER of FeCoNiNC in different metal-site. e) Volcano plot of the ORR overpotential as a function of binding energy for immediate OH*.

commercial RuO_2 catalysts show that the overpotential of both catalysts at 10 mA cm^{-2} was unchanged before and after the 5000 cycle CV test, and the OER performance of Fe$_{3\%}$Co$_{3\%}$Ni$_{9\%}$-NC1000 catalyst was almost the same as that of commercial noble metal catalyst, indicating the excellent durability of electrocatalyst in alkaline solution (Fig. 4g). The chronopotentiometry curve was further tested (Fig. S22a), showing the catalyst can retained up to 87% of its original current after undergoing 20 h. After the stability test, the η_{10} of Fe$_{3\%}$Co$_{3\%}$Ni$_{9\%}$-NC1000 only decreased by 20 mV (Fig. S22b). The potential difference (ΔE) between the ORR half-wave potential and the η_{10} of the OER is 0.633 V, which is much better than the other prepared catalysts. many of the currently reported catalysts (Fig. 4h). The comparison of the ΔE and ORR durability of Fe$_{3\%}$Co$_{3\%}$Ni$_{9\%}$-NC1000 with the bifunctional oxygen catalysts reported recently has presented in Fig. 4i and Table S5, the as-obtained Fe$_{3\%}$Co$_{3\%}$Ni$_{9\%}$-NC1000 show strong competition in terms of ΔE and ORR stability time, such as Fe, Co, N-C (0.74 V, 20 h) [48], Fe$_1$Co$_1$-CNF (0.86 V, 1000 s) [49], Fe-N @ Ni-HCFs (0.687 V, 12 h) [50] and Co-CoN$_4$ @NCNs (0.71 V, 12 h) [51]. Fe$_{3\%}$Co$_{3\%}$Ni$_{9\%}$-NC1000 demonstrated the most efficient activity and the longest persistence among the reported oxygen catalysts. The excellent ORR and OER durability of Fe$_{3\%}$Co$_{3\%}$Ni$_{9\%}$-NC1000 can be derived from its trimetallic single-atoms synergistic effect and the high degree of graphitization. These above results prove that Fe$_{3\%}$Co$_{3\%}$Ni$_{9\%}$-NC1000 catalyst can effectively promote the ORR and OER processes under alkaline conditions.

3.3. Catalytic mechanism of the ORR/OER

DFT calculations were performed to gain insight into the origin of the enhanced activity of the trimetallic single-atoms catalyst. We started with the calculation of the formation energy (E$_f$) of monometallic, bimetallic, and trimetallic single-atoms electrocatalysts (Fig. 5a and S23). It is found that the E$_f$ of all these catalysts are negative, implying that all the structures are thermodynamically stable. The E$_f$ for FeNC, CoNC, NiNC, FeCoNC, FeNiNC, and CoNiNC is -3.79, -4.28, -4.54, -6.55, -6.29, and -7.31, respectively. Compared with these monometallic and bimetallic single-atom structures, the trimetallic single-atoms model shows the most negative formation energy, suggesting that the formation of the FeCoNiNC is more energetically favorable. Partial density of states (PDOS) and d-band structures of FeNC, CoNC, NiNC, FeCoNC, FeNiNC, CoNiNC, and FeCoNiNC are illustrated in Fig. 5b and S23b-d. In comparison with monometallic and bimetallic single-atom structures, the d-band center of the FeCoNiNC shifts toward the Fermi level. Based on the d-band theory, the upshift of d-band center can result in less electron filling in the antibonding orbital, and thus promote the absorption of the reaction intermediates of O*, OH*, OOH* on the FeCoNiNC surface [52,53]. It is noticeable the more occupied electron states at the around the Fermi level of Fe, Co, and Ni atoms in FeCoNiNC than these atoms in monometallic and bimetallic single-atom structures. Fig. S24 portrayed the d-band center for monometallic (Fe, Co, and Ni). The d-band centers of both Fe and Co in FeCoNiNC are shifted towards the Fermi level compared to the comparison sample. This optimized adsorption strength of oxygen-containing intermediates serves as the foundation for further calculations of Fe and Co as active centers for ORR and OER, respectively. Fig. S25, 26 show the differential charge density of all structures, where yellow represents the charge accumulation area and cyan represents the charge depletion area. It is observed that all structures have obvious electron transfer between the transition metal atoms and coordinated N atoms. Compared with monometallic and bimetallic single-atom structures, there is trimetallic synergistic modulation in FeCoNiNC, which may be favorable for the catalytic reactions.

As shown in Fig. S27-29, the oxygen adsorption model and adsorption energy on the catalyst surface suggest that the FeCoNiNC catalyst has the strongest oxygen adsorption energy, which will be beneficial for the oxygen mediated process. Fig. 5c, d, and S30–32 illustrate the free energy diagrams of oxygenated intermediates on these structures. The

free energy paths of ORR for most structures present a consistent downhill tendency at U = 0 V, implying the stable exothermal process, except for NiNC, CoNiNC-Ni site, and FeCoNiNC-Ni site. At the equilibrium potential of 0.86 V, the highest free energy change (ΔG) of Fe, Co, and Ni sites in the FeCoNiNC model are 0.15 eV (O* $\rightarrow$ OH*), 0.51 eV (O$_2$ $\rightarrow$ OOH*), and 0.94 eV (O$_2$ $\rightarrow$ OOH*) (Table S6, 7), revealing that the ORR catalytically active center is mainly the Fe site. The highest ΔG values for both the monometallic single-atom and bimetallic single-atom structures exceed 0.15 eV, indicating that the trimetallic synergistic effect results in an optimal reaction route for FeCoNiNC. For the OER pathway, the largest ΔG of Fe, Co, and Ni sites for the FeCoNiNC catalyst are 1.03 eV (O* $\rightarrow$ OOH*), 0.33 eV (O* $\rightarrow$ OOH*), and 0.96 eV (H$_2$O $\rightarrow$ OH*) at 1.23 V, revealing that the OER catalytically active center is mainly the Co site (Table S8, 9). Similar to the ORR system, the ΔG of the catalytic site in FeCoNiNC is smaller than that of both monometallic single-atom and bimetallic single-atom structures. To visualize the scaling relationship between metal sites and ORR kinetics in metal single-atom catalysts, the descriptor ΔE_{OH*} displays a volcano relationship with ORR overpotential at 0.86 V (Fig. 5e). Monometallic single-atom adsorption to OH* fluctuates in strength and can be portrayed as NiNC < CoNC < FeNC. Due to the synergistic effect between the metals, bimetallic single-atom catalysts modify the adsorption energy of OH*. More inspiring, when the three metals Fe, Co, and Ni are present together, the weakly adsorbed Co and Ni regulate the adsorption of Fe, which is highly adsorbed with OH*, to an $\Delta E_{OH*} \approx 0$. The nearly zero OH* adsorption energy at the Fe site in FeCoNiNC indicates that the tri-metal monoatomic synergistic effect donates the most excellent ORR kinetics of FeCoNiNC. As shown in Fig. S33, the descriptors E$_{O*}$ and E$_{OOH*}$ also revealed the volcano relationship with the ORR overpotential at 0.86 V. The descriptor ΔE_{OH*} for ORR/OER electrocatalytic not only supplies a theoretical basis for this study, but also provide a design principle for the subsequent construction of multi-metallic single-atom bifunctional electrocatalysts.

3.4. Low-temperature flexible Zn-air battery with Fe$_x$Co$_y$Ni$_z$-NC

Based on the excellent ORR and OER performance of the Fe$_{3\%}$Co$_{3\%}$Ni$_{9\%}$-NC1000 catalyst, the FZABs were assembled by pressing the catalysts loaded gas diffusion layer, and copper mesh (current collector) as the air cathode, the KOH saturated PAA gel as the quasi-solid electrolyte and the zinc plate as the metal anode. The schematic structure of the FZABs is shaped like a sandwich (Fig. 6a). The optimized catalyst loading with 10 mg cm^{-2} was determined by comparison from 2 to 15 mg cm^{-2} (Fig. S34), and the battery with gas diffusion layer at the cathode exhibited the best performance (Fig. S35). Based on the optimized design, the performance of the FZABs with Fe$_{3\%}$Co$_{3\%}$Ni$_{9\%}$-NC1000 and commercial Pt/C+RuO$_2$ cathodes were compared, it is apparent that the FZAB with Fe$_{3\%}$Co$_{3\%}$Ni$_{9\%}$-NC1000 shows the improved open circuit voltage (about 1.5 V), and a much smaller charge-discharge voltage gap, confirming the excellent performance of Fe$_{3\%}$Co$_{3\%}$Ni$_{9\%}$-NC1000 catalyst-based FZABs (Fig. S36). Fe$_{3\%}$Co$_{3\%}$Ni$_{9\%}$-NC1000 catalyst-based FZAB shows a more obvious advantage at power density (291.2 mW cm^{-2} at room temperature), which is 1.55 times higher than that of the Pt/C+RuO$_2$-based FZAB (Fig. 6b). Even at the -15 ℃, the power density of FZAB can still reach more than 60 mW cm^{-2}, which further proves the excellent electrocatalytic performance of the catalyst (Fig. 6c). Fig. 6d shows the EIS curves of the FZABs with Fe$_{3\%}$Co$_{3\%}$Ni$_{9\%}$-NC1000 and Pt/C+RuO$_2$ catalysts, the small charge transfer resistances of Fe$_{3\%}$Co$_{3\%}$Ni$_{9\%}$-NC1000 benefits for polarization reducing inside the FZAB. Fig. S37 displays the FZAB equivalent circuit diagram. Moreover, EIS analyses were performed on the FZABs with the Fe$_{3\%}$Co$_{3\%}$Ni$_{9\%}$-NC1000 and Pt/C+ RuO$_2$ electrocatalyst at -15 ℃. As exhibited in Fig. S38, the internal impedance and charge transfer impedance of the noble metal-based FZAB are still greater than those of the Fe$_{3\%}$Co$_{3\%}$Ni$_{9\%}$-NC1000-based FZAB. Specifically, the internal resistance of FZAB with the Fe$_{3\%}$Co$_{3\%}$Ni$_{9\%}$-NC1000 catalyst is
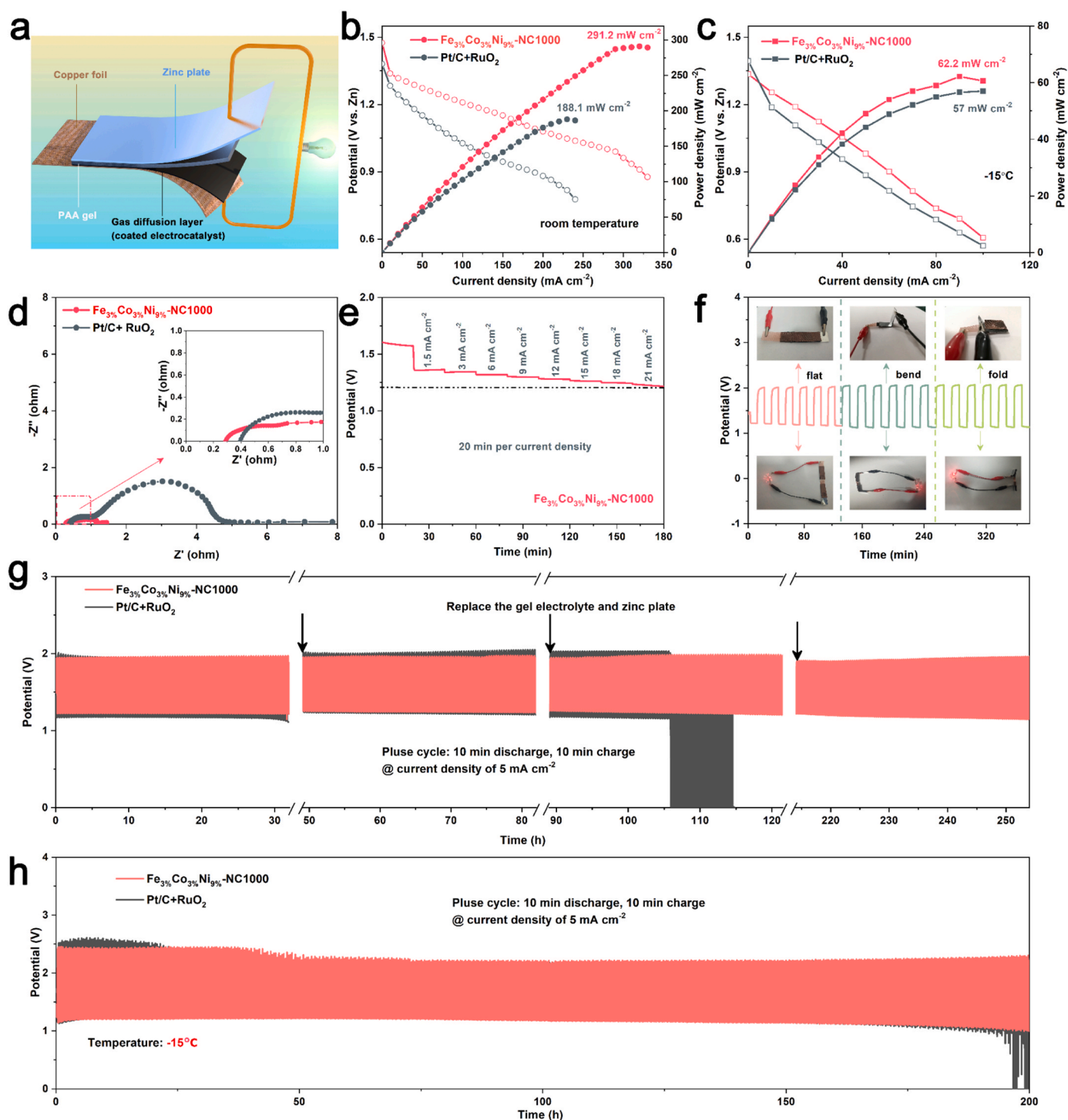
Fig. 6. Performance of FZAB using the $Fe_{3\%}Co_{3\%}Ni_{9\%}$-NC1000 catalyst. a) Schematic diagram of the $Fe_{3\%}Co_{3\%}Ni_{9\%}$-NC1000 catalyst-based FZAB. b) Polarization curves and corresponding power density plots at room temperature. c) Polarization curves and corresponding power density plots at −15 °C. d) Nyquist plots of the impedance of $Fe_{3\%}Co_{3\%}Ni_{9\%}$-NC1000 and Pt/C+RuO$_2$ catalysts-based FZABs. e) Discharge curves of the FZAB based on $Fe_{3\%}Co_{3\%}Ni_{9\%}$-NC1000 at different current densities. f) Charge-discharge cycling performance of FZAB based on $Fe_{3\%}Co_{3\%}Ni_{9\%}$-NC1000 electrocatalyst at a constant charge-discharge current density of 5 mA cm^{-2} under different bending states. Charge-discharge cycling performance of FZAB based on $Fe_{3\%}Co_{3\%}Ni_{9\%}$-NC1000 electrocatalyst at different temperatures under constant charge-discharge current density of 5 mA cm^{-2} g) room temperature, h) −15 °C.

only 0.29 Ω at room temperature. However, the internal resistance increases to 3.9 Ω at −15 °C, around 13 times that at room temperature. The increased internal resistance leads to higher ohmic polarization and consequently reduced battery performance [54,55]. The internal resistance is directly associated with the inherent ion conductivity of the electrolyte [56]. As expected, the conductivity of the electrolyte at low temperatures was significantly reduced. The poor conductivity of the electrolyte is regarded as one of the main bottlenecks for working FZABs with noble metal-free electrocatalysts at low temperatures. In Table S10, the peak power density of FZABs assembled with $Fe_{3\%}Co_{3\%}$-$Ni_{9\%}$-NC1000 and Pt/C+RuO$_2$ are presented with respect to the catalysts that have been reported recently. The battery performance verified

that the $Fe_{3\%}Co_{3\%}Ni_{9\%}$-NC1000 sample is a promising oxygen catalyst for flexible Zn-air batteries.

Furthermore, FZAB with $Fe_{3\%}Co_{3\%}Ni_{9\%}$-NC1000 cathode still maintains excellent stability at current densities ranging from 1.5 to 21 mA cm^{-2} (Fig. 6e). The discharge potential plateau decreases with increasing current density and remains stable at each current density tested, maintaining 1.21 V even at a relatively high current density of 21 mA cm^{-2}. In addition, Fig. 6f shows the charge-discharge cycling curve of FZABs at different bending states, and the performance of the battery has not been changed by bending. The upper inset image of Fig. 6f shows the FZABs in the flat, bend and fold state, indicating that it has good flexibility. In under inset image of Fig. 6f, two FZABs in series can light up several small LED bulbs with a rated voltage of 3 V. To investigate the stability of batteries, the galvanostatic charge-discharge cycling tests at 5 mA cm^{-2} with each cycle being 20 min. As shown in Fig. 6g, the $Fe_{3\%}Co_{3\%}Ni_{9\%}$-NC1000 catalyst-based FZAB showed higher discharge potential ($\approx$ 1.25 V), lower charge potential ($\approx$ 1.95 V), and longer cycle times (more than 250 h) than those of Pt/C+RuO$_2$ catalyst-based FZABs ($\approx$ 1.15 V, $\approx$ 2.05 V, and more than 150 h, respectively). This result is consistent with the discharge-charge polarization curve, which also shows that the $Fe_{3\%}Co_{3\%}Ni_{9\%}$-NC1000 catalyst-based FZABs have excellent battery performance. Furthermore, the $Fe_{3\%}Co_{3\%}Ni_{9\%}$-NC1000 catalyst-based FZABs show much better cycling stability, with no significant decrease in the potential gap within 750 cycles for 250 h while the Pt/C+RuO$_2$ catalyst-based FZAB exhibits an increasing potential gap. What is more worth mentioning is that at -15 ℃, the charge-discharge cycle can reach 200 h without changing the gel and zinc sheet of the $Fe_{3\%}Co_{3\%}Ni_{9\%}$-NC1000 catalyst-based FZAB (Fig. 6h). At the beginning of the cycle, because the temperature is too low, the charging voltage platform of FZABs reaches 2.4 V, but when FZABs is stable at low temperature, the charging voltage platform is stable at 2.2 V. Low-temperature FZABs have surprising long-term stability. The excellent performance of FZABs is closely related to the trimetallic single-atoms synergy effect, hierarchical porous structure, and high bifunctional performance of the catalyst. The battery performance verified that the $Fe_{3\%}Co_{3\%}Ni_{9\%}$-NC1000 catalyst is a promising bifunctional air electrode for flexible Zn-air batteries.

4. Conclusion

In summary, we have constructed the trimetallic single-atoms electrocatalyst as a model for systematic investigation of ORR/OER kinetics. The $Fe_{3\%}Co_{3\%}Ni_{9\%}$-NC1000 displayed remarkable catalytic activity and stability, with bifunctional ORR and OER performance (ORR: $E_{1/2}$ = 0.927 V, OER: $E_{j=10}$ = 1.56 V, ΔE=0.633 V) and 95% stability after 100 h, which outperformed the state-of-the-art Pt/C–RuO$_2$ hybrid. Meanwhile, the FZABs with $Fe_{3\%}Co_{3\%}Ni_{9\%}$-NC1000 exhibited high power density (62.2 mW cm^{-2} at -15 °C, 291.2 mW cm^{-2} at 25 °C) and long-term durability (200 h at -15 °C, over 250 h at room temperature). The catalyst after pyrolysis produces some mesopores and macropores due to the volatilization of zinc, forming a hierarchical porous structure, which facilitates the transport of gas and electrolytes. Density functional theory (DFT) calculations reveal that the ORR and OER catalytically active sites of $Fe_{3\%}Co_{3\%}Ni_{9\%}$-NC1000 are Fe and Co sites, respectively. The description of ΔE_{OH^*} exhibiting a volcano-like relationship with the ORR overpotential explains the remarkable catalytic activity of the trimetallic single-atom catalyst. The presence of Ni sites modulates the coordination environment and electronic structure of Fe and Co sites, resulting in superior adsorption strength of oxygenated intermediates, lessened reaction energy barriers, and accelerated kinetics of oxygen redox reactions. Within this system, the trimetallic single-atoms synergy effect tunes the d-band center of the metals to further interpret the efficacious bifunctionality of the catalyst. Exploiting the unique ORR/OER electrocatalytic performance, the heteroatom coordination-based air electrodes exhibit much improved low-temperature adaptability, power density, and cycling stability, suggesting the electrocatalytic

approach represents a promising strategy to tackle the fundamental challenges facing flexible Zn-air batteries.

CRediT authorship contribution statement

Wenfang Zhai: Conceptualization, Investigation, Data curation, Writing – original draft. **Yuting He:** Formal analysis, Data curation. **Yu-e Duan:** Formal analysis, Data curation. **Shengwu Guo:** Visualization, Resoures. **Yuanzhen Chen:** Visualization, Supervision. **Zhengfei Dai:** Formal analysis, Visualization, Resoures. **Liting Liu:** Resources, Supervision, Writing – review & editing. **Qiang Tan:** Writing – review & editing, Project administration, Supervision, Funding acquisition.

Declaration of Competing Interest

The authors declare that they have no known competing financial interests or personal relationships that could have appeared to influence the work reported in this paper.

Data availability

Data will be made available on request.

Appendix A. Supporting information

Supplementary data associated with this article can be found in the online version at doi: 10.1016/j.apcatb.2023.xxxxxx.

Appendix A. Supporting information

Supplementary data associated with this article can be found in the online version at doi:10.1016/j.apcatb.2023.123438.

References

[1] S.S. Shinde, J.Y. Jung, N.K. Wagh, C.H. Lee, D.-H. Kim, S.-H. Kim, S.U. Lee, J.-H. Lee, Ampere-hour-scale zinc–air pouch cells, Nat. Energy 6 (2021) 592–604, https://doi.org/10.1038/s41560-021-00807-8.

[2] M. Xu, H. Dou, Z. Zhang, Y. Zheng, B. Ren, Q. Ma, G. Wen, D. Luo, A. Yu, L. Zhang, X. Wang, Z. Chen, Hierarchically nanostructured solid-state electrolyte for flexible rechargeable zinc–air batteries, Angew. Chem. Int. Ed. 61 (2022), e202117703, https://doi.org/10.1002/anie.202117703.

[3] T. Zhang, N. Wu, Y. Zhao, X. Zhang, J. Wu, J. Weng, S. Li, F. Huo, W. Huang, Frontiers and structural engineering for building flexible zinc-air batteries, Adv. Sci. 9 (2022), 2103954, https://doi.org/10.1002/advs.202103954.

[4] X. Xiao, Z. Zheng, X. Zhong, R. Gao, Z. Piao, M. Jiao, G. Zhou, Rational design of flexible Zn-based batteries for wearable electronic devices, ACS Nano 17 (2023) 1764–1802, https://doi.org/10.1021/acsnano.2c09509.

[5] X. Fan, H. Wang, X. Liu, J. Liu, N. Zhao, C. Zhong, W. Hu, J. Lu, Functionalized nanocomposite gel polymer electrolyte with strong alkaline-tolerance and high zinc anode stability for ultralong-life flexible zinc–air batteries, Adv. Mater. 35 (2023), 2209290, https://doi.org/10.1002/adma.202209290.

[6] J.-N. Liu, C.-X. Zhao, J. Wang, D. Ren, B.-Q. Li, Q. Zhang, A brief history of zinc-air batteries: 140 years of epic adventures, Energy Environ. Sci. 15 (2022) 4542–4553, https://doi.org/10.1039/D2EE02440C.

[7] W. Sun, F. Wang, B. Zhang, M. Zhang, V. Küpers, X. Ji, C. Theile, P. Bieker, K. Xu, C. Wang, M. Winter, A rechargeable zinc-air battery based on zinc peroxide chemistry, Science 371 (2021) 46–51, https://doi.org/10.1126/science.abb9554.

[8] Y. Li, S.H. Talib, D. Liu, K. Zong, A. Saad, Z. Song, J. Zhao, W. Liu, F. Liu, Q. Ji, P. Tsiakaras, X. Cai, Improved oxygen evolution reaction performance in $Co_{0.4}Mn_{0.6}O_2$ nanosheets through triple-doping (Cu, P, N) strategy and its application to Zn-air battery, Appl. Catal. B-Environ. 320 (2023), 122023, https://doi.org/10.1016/j.apcatb.2022.122023.

[9] X. Zheng, Y. Cao, H. Wang, J. Zhang, M. Zhao, Z. Huang, Y. Wang, L. Zhang, Y. Deng, W. Hu, X. Han, Designing breathing air-electrode and enhancing the oxygen electrocatalysis by thermoelectric effect for efficient Zn-air batteries, Angew. Chem. Int. Ed. 62 (2023), e202302689, https://doi.org/10.1002/anie.202302689.

[10] Y. He, X. Yang, Y. Li, L. Liu, S. Guo, C. Shu, F. Liu, Y. Liu, Q. Tan, G. Wu, Atomically dispersed Fe–Co dual metal sites as bifunctional oxygen electrocatalysts for rechargeable and flexible Zn–air batteries, ACS Catal. 12 (2022) 1216–1227, https://doi.org/10.1021/acscatal.1c04550.

[11] H. Wang, L. Xu, D. Deng, X. Liu, H. Li, D. Su, Regulated electronic structure and improved electrocatalytic performances of S-doped $FeWO_4$ for rechargeable zinc-air batteries, J. Energy Chem. 76 (2023) 359–367, https://doi.org/10.1016/j.jechem.2022.09.023.

[12] X. Yan, D. Deng, S. Wu, H. Li, L. Xu, Development of transition metal nitrides as oxygen and hydrogen electrocatalysts, Chin. J. Struct. Chem. 41 (2022) 2207004, https://doi.org/10.14102/j.cnki.0254-5861.2022-0036.

[13] Y. He, X. Zhou, Y. Jia, H. Li, Y. Wang, Y. Liu, Q. Tan, Advances in transition-metal-based dual-atom oxygen electrocatalysts, Small (2023), 2206477, https://doi.org/10.1002/smll.202206477.

[14] D. Deng, H. Ma, S. Wu, H. Wang, J. Qian, J. Wu, H. Li, C. Yan, H. Li, L. Xu, Engineering electronic density and coordination environment of Mn–N_x sites via Zn cooperation for quasi-solid-state zinc-air batteries, Renewables 1 (2023) 362–372, https://doi.org/10.31635/renewables.023.202200020.

[15] D. Deng, S. Wu, H. Li, H. Li, L. Xu, P-orbital bismuth single-atom catalyst for highly effective oxygen electroreduction in quasi-solid zinc-air batteries, Small 19 (2023), 2205469, https://doi.org/10.1002/smll.202205469.

[16] X. Han, N. Li, J.S. Baik, P. Xiong, Y. Kang, Q. Dou, Q. Liu, J.Y. Lee, C.S. Kim, H. S. Park, Sulfur mismatch substitution in layered double hydroxides as efficient oxygen electrocatalysts for flexible zinc–air batteries, Adv. Funct. Mater. 33 (2023), 2212233, https://doi.org/10.1002/adfm.202212233.

[17] C. Zhou, X. Chen, S. Liu, Y. Han, H. Meng, Q. Jiang, S. Zhao, F. Wei, J. Sun, T. Tan, R. Zhang, Superdurable bifunctional oxygen electrocatalyst for high-performance zinc–air batteries, J. Am. Chem. Soc. 144 (2022) 2694–2704, https://doi.org/10.1021/jacs.1c11675.

[18] L. Zheng, C. Jiang, M. Zheng, X. Peng, T. Liu, S. Xi, X. Chi, Q. Zhang, L. Gu, S. Zhang, G. Shi, L. Zhang, K. Wu, Z. Chen, T. Li, M. Dahbi, J. Alami, K. Amine, J. Lu, Wood carbon based single-atom catalyst for rechargeable Zn–air batteries, ACS Energy Lett. 6 (2021) 3624–3633, https://doi.org/10.1021/acsenergylett.1c01678.

[19] M. Zhao, H. Liu, H. Zhang, W. Chen, H. Sun, Z. Wang, B. Zhang, L. Song, Y. Yang, C. Ma, Y. Han, W. Huang, A pH-universal ORR catalyst with single-atom iron sites derived from a double-layer MOF for superior flexible quasi-solid-state rechargeable Zn–air batteries, Energy Environ. Sci. 14 (2021) 6455–6463, https://doi.org/10.1039/D1EE01602D.

[20] Z. Zhang, T. Wang, W. Wang, S. Wang, X. Luo, C. Cheng, X. Liu, A stable imide-linked metalphthalocyanine framework with atomically dispersed Fe-N_4 sites and ultrafine nickel oxide nanoparticles to boost reversible oxygen electrocatalysis with a record-low ΔE of 0.59 V, Adv. Energy Mater. 13 (2023), 2300325, https://doi.org/10.1002/aenm.202300325.

[21] X. Li, X. Yang, L. Liu, H. Zhao, Y. Li, H. Zhu, Y. Chen, S. Guo, Y. Liu, Q. Tan, G. Wu, Chemical vapor deposition for N/S-doped single Fe site catalysts for the oxygen reduction in direct methanol fuel cells, ACS Catal. 11 (2021) 7450–7459, https://doi.org/10.1021/acscatal.0c05446.

[22] Y. He, Y. Jia, B. Yu, Y. Wang, H. Li, Y. Liu, Q. Tan, Heteroatom coordination regulates iron single-atom-catalyst with superior oxygen reduction reaction performance for aqueous Zn-air battery, Small 19 (2023), 2206478, https://doi.org/10.1002/smll.202206478.

[23] B. Chi, L. Zhang, X. Yang, Y. Zeng, Y. Deng, M. Liu, J. Huo, C. Li, X. Zhang, X. Shi, Y. Shao, L. Gu, L. Zheng, Z. Cui, S. Liao, G. Wu, Promoting ZIF-8-derived Fe–N–C oxygen reduction catalysts via Zr doping in proton exchange membrane fuel cells: durability and activity enhancements, ACS Catal. 13 (2023) 4221–4230, https://doi.org/10.1021/acscatal.2c06118.

[24] L. Liu, A. Corma, Evolution of isolated atoms and clusters in catalysis, Trends Chem. 2 (2020) 383–400, https://doi.org/10.1016/j.trechm.2020.02.003.

[25] J. Yang, H. Qi, A. Li, X. Liu, X. Yang, S. Zhang, Q. Zhao, Q. Jiang, Y. Su, L. Zhang, J.-F. Li, Z.-Q. Tian, W. Liu, A. Wang, T. Zhang, Potential-driven restructuring of Cu single atoms to nanoparticles for boosting the electrochemical reduction of nitrate to ammonia, J. Am. Chem. Soc. 144 (2022) 12062–12071, https://doi.org/10.1021/jacs.2c02262.

[26] B. Xi, X. Sun, Single-atom catalysts electrostatically stabilized by ionic liquids, Chem 5 (2019) 3012–3014, https://doi.org/10.1016/j.chempr.2019.11.013.

[27] D. Deng, J. Qian, X. Liu, H. Li, D. Su, H. Li, H. Li, L. Xu, Non-covalent interaction of atomically dispersed Cu and Zn pair sites for efficient oxygen reduction reaction, Adv. Funct. Mater. 32 (2022), 2203471, https://doi.org/10.1002/adfm.202203471.

[28] H. Wang, H. You, G. Wu, L. Huang, J. Yan, X. Liu, Y. Ma, M. Wu, Y. Zeng, J. Yu, H. Zhang, Co/Fe co-doped ZIF-8 derived hierarchically porous composites as high-

[29] H. Chen, K. Shen, Y. Tan, Y. Li, Multishell hollow metal/nitrogen/carbon dodecahedrons with precisely controlled architectures and synergistically enhanced catalytic properties, ACS Nano 13 (2019) 7800–7810, https://doi.org/10.1021/acsnano.9b01953.

[30] Y. Hu, C. Chen, T. Shen, X. Guo, C. Yang, D. Wang, Y. Zhu, Hollow carbon nanorod confined single atom Rh for direct formic acid electrooxidation, Adv. Sci. 9 (2022), 2205299, https://doi.org/10.1002/advs.202205299.

[31] T. Cui, Y.-P. Wang, T. Ye, J. Wu, Z. Chen, J. Li, Y. Lei, D. Wang, Y. Li, Engineering dual single-atom sites on 2D ultrathin N-doped carbon nanosheets attaining ultra-low-temperature zinc-air battery, Angew. Chem. Int. Ed. 61 (2022), e202115219, https://doi.org/10.1002/anie.202115219.

[32] Y. Jiang, Y.-P. Deng, R. Liang, J. Fu, D. Luo, G. Liu, J. Li, Z. Zhang, Y. Hu, Z. Chen, Multidimensional ordered bifunctional air electrode enables flash reactants shuttling for high-energy flexible Zn-air batteries, Adv. Energy Mater. 9 (2019), 1900911, https://doi.org/10.1002/aenm.201900911.

[33] R. Wu, J. Xu, C.-L. Zhao, X.-Z. Su, X.-L. Zhang, Y.-R. Zheng, F.-Y. Yang, X.-S. Zheng, J.-F. Zhu, J. Luo, W.-X. Li, M.-R. Gao, S.-H. Yu, Dopant triggered atomic configuration activates water splitting to hydrogen, Nat. Commun. 14 (2023), 2306, https://doi.org/10.1038/s41467-023-37641-3.

[34] L. Yin, S. Zhang, M. Sun, S. Wang, B. Huang, Y. Du, Heteroatom-driven coordination fields altering single cerium atom sites for efficient oxygen reduction reaction, Adv. Mater. 35 (2023), 2302485, https://doi.org/10.1002/adma.202302485.

[35] Y. Li, J. Li, J. Huang, J. Chen, Y. Kong, B. Yang, Z. Li, L. Lei, G. Chai, Z. Wen, L. Dai, Y. Hou, Boosting electroreduction kinetics of nitrogen to ammonia via tuning electron distribution of single-atomic iron sites, Angew. Chem. Int. Ed. 60 (2021) 9078–9085, https://doi.org/10.1002/anie.202100526.

[36] S. Chen, J. Chen, X. Liao, Y. Li, W. Wang, R. Huang, T. Zhao, S. Yan, Z. Yan, F. Cheng, H. Wang, Enabling low-temperature and high-rate Zn metal batteries by activating Zn nucleation with single-atomic sites, ACS Energy Lett. 7 (2022) 4028–4035, https://doi.org/10.1021/acsenergylett.2c02042.

[37] J. Mo, Y. Ko, Y.S. Yun, J. Huh, J. Cho, A carbonization/interfacial assembly-driven electroplating approach for water-splitting textile electrodes with remarkably low overpotentials and high operational stability, Energy Environ. Sci. 15 (2022) 3815–3829, https://doi.org/10.1039/D2EE01510B.

[38] S. Li, S. Zhao, X. Lu, M. Ceccato, X.-M. Hu, A. Roldan, J. Catalano, M. Liu, T. Skrydstrup, K. Daasbjerg, Low-valence $Zn^{\delta+}$ (0<δ<2) single-atom material as highly efficient electrocatalyst for CO_2 reduction, Angew. Chem. Int. Ed. 60 (2021) 22826–22832, https://doi.org/10.1002/anie.202107550.

[39] L. Jiao, J. Zhu, Y. Zhang, W. Yang, S. Zhou, A. Li, C. Xie, X. Zheng, W. Zhou, S.-H. Yu, H.-L. Jiang, Non-bonding interaction of neighboring Fe and Ni single-atom pairs on MOF-derived N-doped carbon for enhanced CO_2 electroreduction, J. Am. Chem. Soc. 143 (2021) 19417–19424, https://doi.org/10.1021/jacs.1c08050.

[40] C. Liu, Y. Wu, K. Sun, J. Fang, A. Huang, Y. Pan, W.-C. Cheong, Z. Zhuang, Z. Zhuang, Q. Yuan, H.L. Xin, C. Zhang, J. Zhang, H. Xiao, C. Chen, Y. Li, Constructing FeN_4/graphitic nitrogen atomic interface for high-efficiency electrochemical CO_2 reduction over a broad potential window, Chem 7 (2021) 1297–1307, https://doi.org/10.1016/j.chempr.2021.02.001.

[41] Y. Xu, R. Xie, Q. Li, J. Feng, H. Luo, Q. Ye, Z. Guo, Y. Cao, M. Palma, G. Chai, M.-M. Titirici, C.R. Jones, Pyridine functionalized carbon nanotubes: unveiling the role of external pyridinic nitrogen sites for oxygen reduction reaction, Small (2023), 2302795, https://doi.org/10.1002/smll.202302795.

[42] L.-J. Yuan, B. Liu, L.-x Shen, Y.-K. Dai, Q. Li, C. Liu, W. Gong, X.-L. Sui, Z.-B. Wang, d-orbital electron delocalization realized by axial Fe_4C atomic clusters delivers high-performance Fe–N–C catalysts for oxygen reduction reaction, Adv. Mater. 35 (2023), 2305945, https://doi.org/10.1002/adma.202305945.

[43] X. Hu, S. Chen, L. Chen, Y. Tian, S. Yao, Z. Lu, X. Zhang, Z. Zhou, What is the real origin of the activity of Fe–N–C electrocatalysts in the O_2 reduction reaction? critical roles of coordinating pyrrolic N and axially adsorbing species, J. Am. Chem. Soc. 144 (2022) 18144–18152, https://doi.org/10.1021/jacs.2c08743.

[44] X. Zhang, X. Xu, S. Yao, C. Hao, C. Pan, X. Xiang, Z.Q. Tian, P.K. Shen, Z. Shao, S. P. Jiang, Boosting electrocatalytic activity of single atom catalysts supported on nitrogen-doped carbon through N coordination environment engineering, Small 18 (2022), 2105329, https://doi.org/10.1002/smll.202105329.

[45] C. Jiao, Z. Xu, J. Shao, Y. Xia, J. Tseng, G. Ren, N. Zhang, P. Liu, C. Liu, G. Li, S. Chen, S. Chen, H.-L. Wang, High-density atomic Fe–N_4/C in tubular, biomass-derived, nitrogen-rich porous carbon as air-electrodes for flexible Zn–air batteries, Adv. Funct. Mater. 33 (2023), 2213897, https://doi.org/10.1002/adfm.202213897.

[46] Y. Liu, Z. Chen, Z. Li, N. Zhao, Y. Xie, Y. Du, J. Xuan, D. Xiong, J. Zhou, L. Cai, Y. Yang, CoNi nanoalloy-Co-N_4 composite active sites embedded in hierarchical porous carbon as bi-functional catalysts for flexible Zn-air battery, Nano Energy 99 (2022), 107325, https://doi.org/10.1016/j.nanoen.2022.107325.

[47] X. Hai, S. Xi, S. Mitchell, K. Harrath, H. Xu, D.F. Akl, D. Kong, J. Li, Z. Li, T. Sun, H. Yang, Y. Cui, C. Su, X. Zhao, J. Li, J. Pérez-Ramírez, J. Lu, Scalable two-step annealing method for preparing ultra-high-density single-atom catalyst libraries, Nat. Nanotechnol. 17 (2022) 174–181, https://doi.org/10.1038/s41565-021-01022-y.

[48] S. Sarkar, A. Biswas, E.E. Siddharthan, R. Thapa, R.S. Dey, Strategic modulation of target-specific isolated Fe,Co single-atom active sites for oxygen electrocatalysis impacting high power Zn–air battery, ACS Nano 16 (2022) 7890–7903, https://doi.org/10.1021/acsnano.2c00547.

[49] Y. Wang, Z. Li, P. Zhang, Y. Pan, Y. Zhang, Q. Cai, S.R.P. Silva, J. Liu, G. Zhang, X. Sun, Z. Yan, Flexible carbon nanofiber film with diatomic Fe-Co sites for efficient

oxygen reduction and evolution reactions in wearable zinc-air batteries, Nano Energy 87 (2021), 106147, https://doi.org/10.1016/j.nanoen.2021.106147.

[50] Y. Tian, Z. Wu, M. Li, Q. Sun, H. Chen, D. Yuan, D. Deng, B. Johannessen, Y. Wang, Y. Zhong, L. Xu, J. Lu, S. Zhang, Atomic modulation and structure design of Fe-N$_4$ modified hollow carbon fibers with encapsulated Ni nanoparticles for rechargeable Zn–air batteries, Adv. Funct. Mater. 32 (2022), 2209273, https://doi.org/10.1002/adfm.202209273.

[51] K. Ding, J. Hu, J. Luo, L. Zhao, W. Jin, Y. Liu, Z. Wu, G. Zou, H. Hou, X. Ji, Robust electronic correlation of Co-CoN$_4$ hybrid active sites for durable rechargeable Zn-air batteries, Adv. Funct. Mater. 32 (2022), 2207331, https://doi.org/10.1002/adfm.202207331.

[52] Q. Sun, X.-H. Li, K.-X. Wang, T.-N. Ye, J.-S. Chen, Inorganic non-carbon supported Pt catalysts and synergetic effects for oxygen reduction reaction, Energy Environ. Sci. 16 (2023) 1838–1869, https://doi.org/10.1039/D2EE03642H.

[53] X. Lin, Q. Li, Y. Hu, Z. Jin, K.M. Reddy, K. Li, X. Lin, L. Ci, H.-J. Qiu, Revealing atomic configuration and synergistic interaction of single-atom-based Zn-Co-Fe trimetallic sites for enhancing oxygen reduction and evolution reactions, Small 19 (2023), 2300612, https://doi.org/10.1002/smll.202300612.

[54] X. Zhong, Z. Zheng, J. Xu, X. Xiao, C. Sun, M. Zhang, J. Ma, B. Xu, K. Yu, X. Zhang, H.-M. Cheng, G. Zhou, Flexible zinc–air batteries with ampere-hour capacities and wide-temperature adaptabilities, Adv. Mater. 35 (2023), 2209980, https://doi.org/10.1002/adma.202209980.

[55] C.-X. Zhao, J.-N. Liu, N. Yao, X. Zeng, A. Chen, P. Dong, Y. Zhang, X. Ma, C. Tang, B.-Q. Li, Q. Zhang, Low-temperature working feasibility of zinc–air batteries with noble metal-free electrocatalysts, Renewables 1 (2023) 73–80, https://doi.org/10.31635/renewables.023.202300026.

[56] C.-X. Zhao, J.-N. Liu, N. Yao, J. Wang, D. Ren, X. Chen, B.-Q. Li, Q. Zhang, Can aqueous zinc–air batteries work at sub-zero temperatures? Angew. Chem. Int. Ed. 60 (2021) 15281–15285, https://doi.org/10.1002/anie.202104171.